TECHNICAL REPORT NO. 11

TO

The Office of Naval Research
Contract No. N000014-91-J-1414

DUCTILE FRACTURE AND FAILURE CRITERIA OF STRUCTURAL STEELS

D. A. KOSS
Department of Materials Science and Engineering
The Pennsylvania State University
University Park, PA 16802

Progress Report for the period
1 April 1995 - 31 March 1996

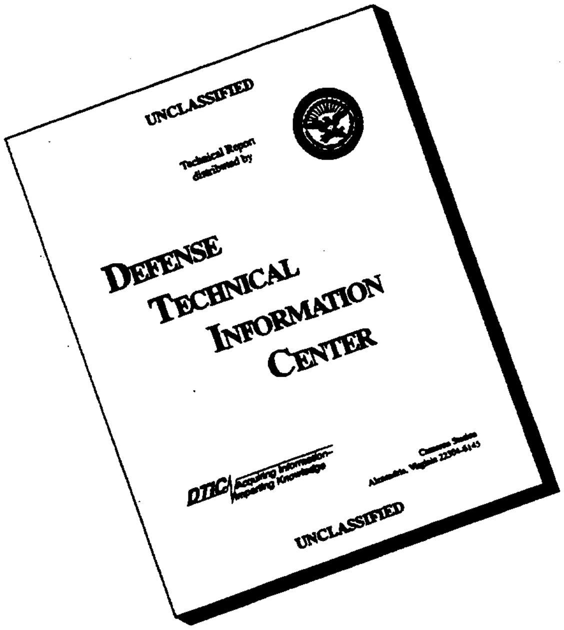
UNCLASSIFIED
Technical Report distributed by
DEFENSE TECHNICAL INFORMATION CENTER
DTIC Acquiring Information— Imparting Knowledge
Cameron Station Alexandria, Virginia 22304-6145
UNCLASSIFIED

REPORT DOCUMENTATION PAGE

Form Approved
OMB No. 0704-0188

1. AGENCY USE ONLY *(Leave blank)*

2. REPORT DATE
June, 1996

3. REPORT TYPE AND DATES COVERED
Annual Report: 4/1/95-3/31/96

4. TITLE AND SUBTITLE
Ductile Fracture and Failure Criteria of Structural Steels

5. FUNDING NUMBERS

6. AUTHOR(S)
D. A. Koss

7. PERFORMING ORGANIZATION NAME(S) AND ADDRESS(ES)
Department of Materials Science and Engineering
Penn State University
University Park, PA 16802

8. PERFORMING ORGANIZATION REPORT NUMBER
Report No. 11

9. SPONSORING/MONITORING AGENCY NAME(S) AND ADDRESS(ES)
Office of Naval Research
800 N. Quincy Street
Arlington, VA

10. SPONSORING/MONITORING AGENCY REPORT NUMBER

11. SUPPLEMENTARY NOTES

12a. DISTRIBUTION/AVAILABILITY STATEMENT
Distribution of this document is unlimited

12b. DISTRIBUTION CODE

13. ABSTRACT *(Maximum 200 words)*

Progress is reviewed for a program which examines multiaxial failure criteria and the associated mechanisms of ductile fracture in structural steels using HY100 as a model system. Failure limit diagram data are presented for the dependence of failure initiation of HY100 over a range of multiaxial tensile stresses and microstructural conditions including material heat treated to simulate heat-affected zone material in a weldment. An analysis of experimental observations suggests two modes of ductile fracture: failure caused by a global accumulation of damage which is very sensitive to stress triaxiality and failure caused by localized void linking in the form of void-stress instabilities which is only moderately sensitive to stress state. A computational model is presented to describe the void-sheet mode of failure while an experimental model has been devised to explore void interaction effects during global damage accumulation.

14. SUBJECT TERMS
Failure criteria, fracture, HY100 steel

15. NUMBER OF PAGES
38

16. PRICE CODE

17. SECURITY CLASSIFICATION OF REPORT

18. SECURITY CLASSIFICATION OF THIS PAGE

19. SECURITY CLASSIFICATION OF ABSTRACT

20. LIMITATION OF ABSTRACT

INTRODUCTION

The structural performance of weldments is often difficult to predict because of their non-uniform microstructures as well as complex geometries. As a result, even under uniaxial loading, the mechanical response of weldments must take into account local stresses which are both multiaxial and spatially non-uniform and are imposed over a range of weldment microstructures (and therefore a range of material properties). Predicting the performance of weldments fabricated from high toughness steels containing small flaws is further complicated by the inapplicability of applying either linear elastic or elastic-plastic fracture mechanics.

An attractive alternate method to predicting weldment performance is to apply a local fracture approach.[1-4] Such an approach relies on the use of accurate constitutive relations to describe flow behavior and multiaxial failure criteria to address failure on a local scale.[5-9] Using computational mechanics techniques, the local fracture approach considers the mechanical response of a small volume element of a weldment under an applied load. Failure of the microscale volume element is dictated by the multiaxial deformation and fracture process and the local failure criterion within that element which in turn is sensitive to local microstructure. Based on a combination of experimental and computational analysis techniques, the present research examines the failure criteria, as well as the failure mechanisms, of HY100 steel weldments under a range of multiaxial tensile stress states. The research seeks to establish the influence of stress state on the failure of steel baseplate and heat-affected zone material in terms of continuum parameters which can be implemented into a computational code describing the mechanical response of a welded joint. The research also seeks to establish the controlling microstructurally-based mechanisms for failure initiation of those steel weldments which are tough, contain physically small flaws, and possess a range of microstructures; in this regard, HY-100 may be considered a model material.

The present research couples closely with research programs at the Naval Surface Warfare Center (Indian Head as well as Annapolis) under the direction of Robert Garrett and Ernest Czyryca. Two students are performing research related to this effort: Dana Goto, Ph.D. candidate, is the graduate student performing the experimental aspects and James Bandstra, who is an Associate

Professor at University of Pittsburgh, Johnstown and employed summers at Concurrent Technology Corporation, Johnstown, is a Ph.D. candidate performing the computational modeling study in this program. This report describes progress for the period 4/1/95 - 3/30/96 for the following projects:

- the influence multiaxial tensile stresses on the failure of HY-100 steel,
- a simulation of void sheet mode of failure, and
- an experimental model of the growth of neighboring voids during ductile fracture.

PROGRAM PROGRESS

1. THE INFLUENCE OF TENSILE STRESS STATE ON THE FAILURE OF HY-100 STEEL

(with D. Goto, Ph.D. Candidate)

The purpose of this aspect of the project is to establish both the conditions for and the mechanisms of failure initiation as a function of stress state for HY-100 steel weldments. The following section describes failure initiation of "conventional" base plate material identified as Plate 1, a low sulfur/inclusion-shape control variant, Plate 2, as well as test specimens subjected to Gleeble thermal cycles to simulate the heat-affected zones in Plate 1. We also wish to emphasize that material failure is defined as that condition in which the material damage is sufficiently severe so that the damage evolution is self-sustaining and causes loss of load-carrying under further deformation.

Materials and Test Procedure

Two plates of HY-100 steel with compositions of Fe-0.16C-2.62Ni-1.32Cr-0.25Mo-0.007S ("Plate 1") and Fe-0.147C-3.05Ni-1.65Cr-0.48Mo-0.001S ("Plate 2") are being studied. Plate 2 has less sulfur and also contains calcium additions for inclusion shape control. Both plate materials received an austenitization at ≈900°C followed by a quench and temper at ≈620°C. This heat treatment produces a microstructure consisting of tempered martensite and bainite; see Figure

1. Plate 1 exhibits microstructural banding, as well as clustering of elongated (30-60 μm long) and equiaxed (1-2 μm diameter) manganese sulfide (MnS) inclusions, parallel to the rolling direction (longitudinal); see Figure 2. Plate 2 has fewer inclusions and these are spheroidal in shape. As well be discussed later, Plate 1 material was also heat treated using a Gleeble thermal cycle simulator in order to simulate heat-affected zone (HAZ) regions formed during multi-pass welding.

Similar to previous studies,[5-7] circumferentially notched and un-notched tensile specimens have been tested. As shown in Fig 3. the notch configurations consisted of a B-Notch ($R/\rho = 0.5$), A-Notch ($R/\rho = 1.0$) and D-Notch ($R/\rho = 2.0$), where 2R is the minimum notch diameter and ρ is the notch root radius. Unless otherwise noted, the specimens were machined such that their applied tensile axes were parallel to the long-transverse (transverse) plate orientation.

Mechanical testing of all specimens was performed at a constant cross-head speed of 1.5 mm/min. This load rate corresponds to an initial strain rate of $10^{-3}s^{-1}$ over a 25 mm gage length in a smooth bar tension test. Load and diametral contraction at the minimum notch diameter were recorded continuously during testing of all notched bars. For smooth bars, axial displacement was monitored up to the onset of necking. Beyond this point diametral contraction at the minimum neck diameter was recorded for the remainder of the test. Testing was performed either to specimen fracture or to a point just prior to fracture (failure initiation).

In addition to tensile testing, compression testing was performed to determine the large strain stress-strain response. Such data were necessary for accurated computational analyses of the local stress states at specimen failure.

Failure Initiation

A key issue in this program is a meaningful definition of failure. In this study, we define a failure load as that point at which the material loses load-carrying capacity due to internal damage (cavitation). This definition implies that, during testing, failure initiation may be taken as the point of discontinuous change in the load-diametral contractions response, whereas fracture refers to physical specimen separation. As an example, Figure 4 shows an abrupt change in the plastic

Figure 1. (a) Light micrograph of the transverse orientation of HY-100 steel base plate
(b) Scanning electron micrograph showing the carbide distribution in the base metal microstructure

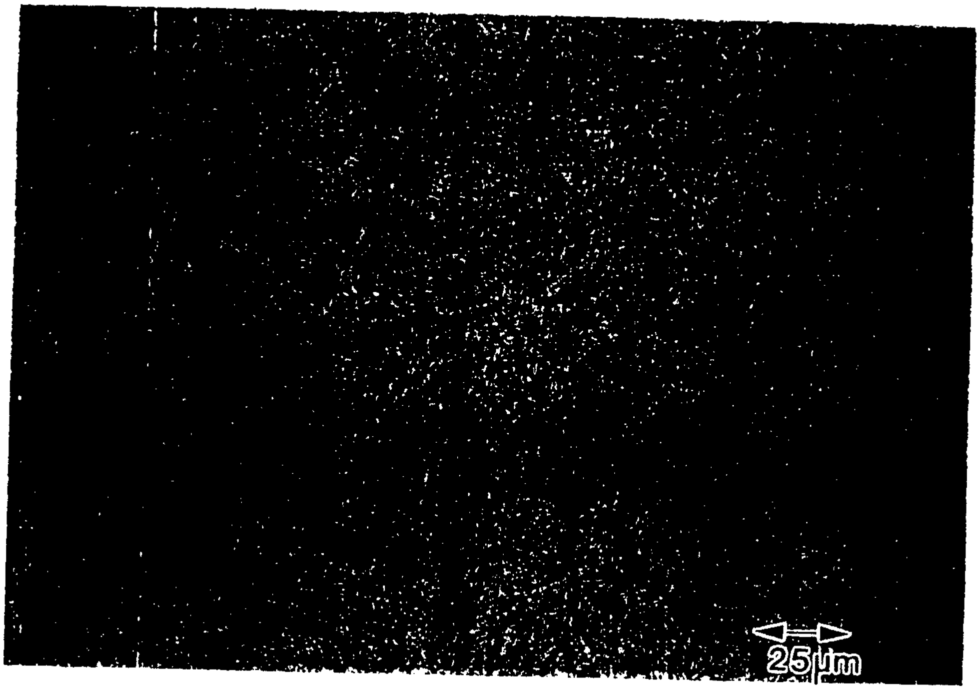

Figure 2. Light micrograph of clustered elongated inclusions in the transverse plane. Inclusion orientation is parallel to the longitudinal direction.

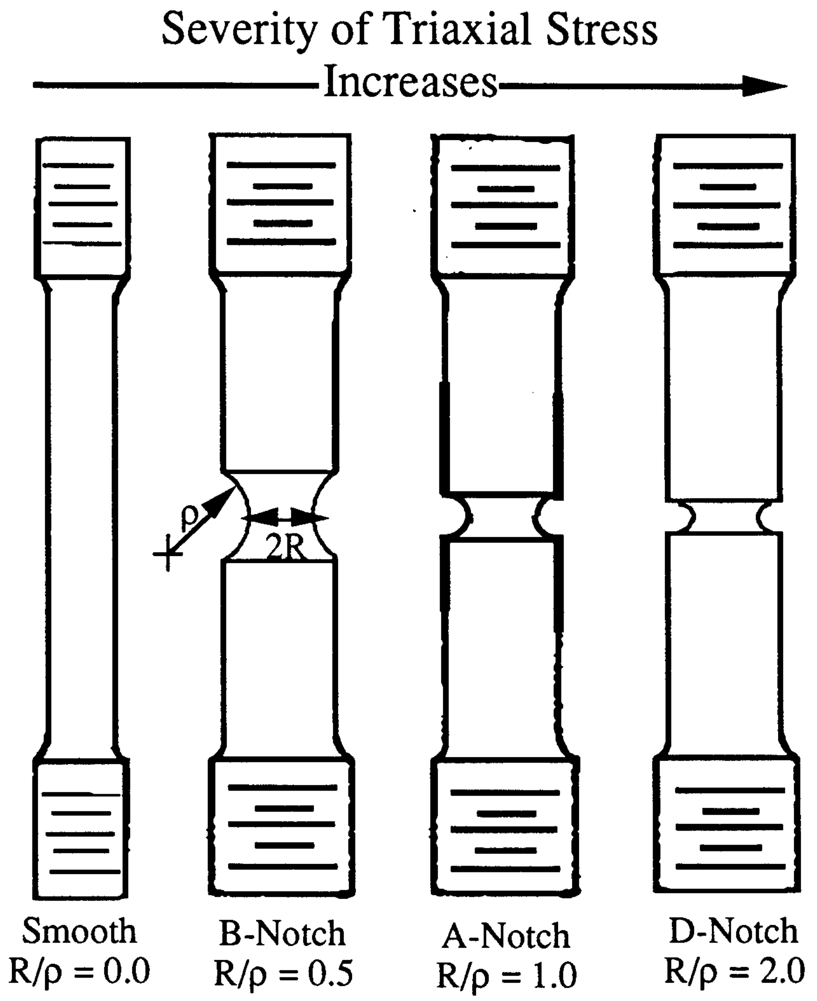

Figure 3. Circumferentially notched and un-notched tensile specimen configurations. The minimum notch diameter (2R) is held constant at 7.62 mm. The radius of curvature of the notch (ρ) is varied in order to achieve the desired R/ρ ratio.

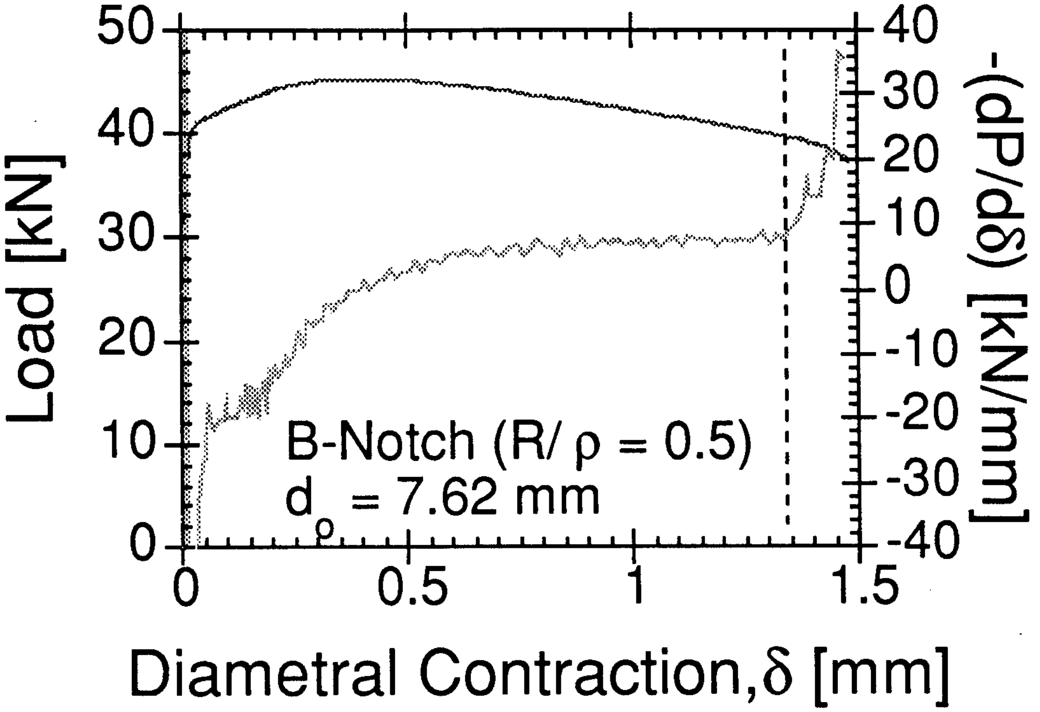

Figure 4. The dependence of load and specimen compliance on diametral contraction. Note rapid change in compliance at failure initiation.

load-deflection response at a displacement of ~135 mm. We interpret this response as indicative of a critical level of damage which has accumulated within the deforming volume such that further deformation causes abrupt increases in the rate of damage accumulation and loss of load-carrying capacity. Thus, the onset of failure is associated with self-propagating damage resulting in catastrophic degradation of the materials's inherent capacity to bear further load. Mechanistically, failure may be associated either by massive void-linking or ductile crack formation at the center of the bar, where stress triaxiality is the greatest.

In conjunction with mechanical testing, finite element analysis (FEA) was utilized to calculate the mean (hydrostatic) stress, σ_m, effective (von Mises) stress, σ_{eff}, and equivalent plastic strain, $\bar{\varepsilon}_{pl}$, values within the specimen throughout deformation. The stress triaxiality ratio, defined as σ_m/σ_{eff}, and $\bar{\varepsilon}_{pl}$ at the failure initiation site, i.e., at the bar center, was used to characterized the stress-strain state condition at failure, as well as to construct a failure limit diagram.

Failure Limit Diagram for Base Metal

The dependency of the failure strain on the stress triaxiality characteristic of the imposed deformation may be depicted in a failure limit diagram. The failure limit diagram for Plates 1 and 2 are illustrated in Figure 5. This figure shows several features:

- a very rapid decrease in failure strain with increasing stress triaxiality for all materials except transverse Plate 1 at high σ_m/σ_{eq}; note Figure 5b.
- while plate orientation influences failure strains significantly at intermediate triaxialities ($\sigma_m/\sigma_{eq} \approx 1$), little effect is observed at high σ_m/σ_{eq}, Figure 5b.
- when compared to transverse Plate 1, the inclusion-control/low sulfur plate, Plate 2, exhibits much higher failure strains at intermediate σ_m/σ_{eq}-values, but only a small improvement at high σ_m/σ_{eq}, Figure 5b
- due to specimen necking, the smooth bar tensile test subjects the material to a large range of stress triaxialities (0.33 to ~ 0.85) prior to "failure", Figure 5a
- As shown in Figure 5b, it appears that the data for the transverse Plate 1 material may be separated into two regions: Region I at low-intermediate stress triaxialities in which the failure strain decreases rapidly with increasing σ_m/σ_{eq} and Region II at high σ_m/σ_{eq} -values in which the failure strains decrease slowly with increasing σ_m/σ_{eq}.

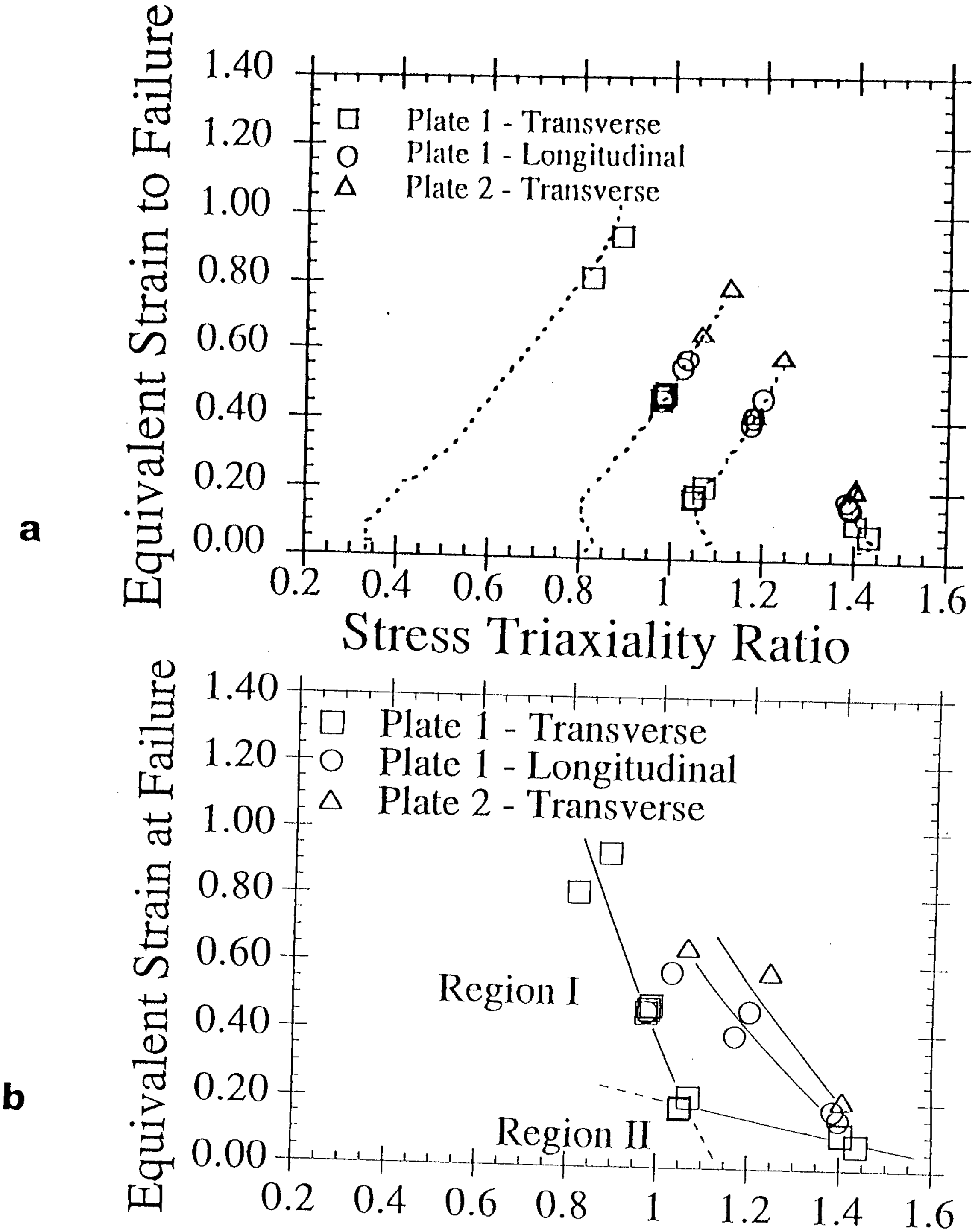

Figure 5. Failure limit diagram for HY-100 steel baseplate. The dotted lines in (a) denote stress path from initial specimen loading to failure while (b) indicates sensitivity of failure strain to stress state.

Taken as a whole, these data tend to imply that at low to moderate levels of imposed triaxiality, e.g., those characterized by smooth, B-Notch ($R/\rho = 0.5$), and A-Notch ($R/\rho = 1.0$), plate chemistry and inclusion orientation can yield significant differences in ductility. For example, in Region I an increase in triaxiality by a factor of ≈ 1.3, from smooth ($R/\rho = 0.0$) to A-Notch ($R/\rho = 1.0$) in Plate 1-Transverse specimens yields a ≈ 5X decrease in failure initiation strain. At higher triaxiality levels, e.g., those characteristic of the D-Notch ($R/\rho = 2.0$) configuration, plate chemistry and orientation appear to have far less influence on failure initiation and ductility.

Failure Mechanism :

In order to gain insight into the fracture mechanism of the transverse Plate 1, specifically the apparent change in sensitivity of the failure strain to stress triaxialities at intermediate σ_m/σ_{eq} values, fractography along with metallographic sectioning was performed. As shown in Figure 6, these observations indicate Plate 1-Transverse specimens with high degrees of notch constraint, e.g., A-Notch ($R/\rho = 1.0$) and D-Notch ($R/\rho = 2.0$) configurations, appear to fail by a "void-sheet" mechanism Region II, characterized by weak sensitivities of strain-to-failure on triaxiality. Fractography of A-Notch and D-Notch specimens reveals the presence of aligned and parallel ridges and valleys of elongated inclusion-nucleated voids connected by inclined planes (≈ 45° to the applied tensile axis) covered by small carbide-nucleated voids. These features are suggestive of a "void-sheet" initiated failure mechanism, and give rise to a "layered" or "zig/zag" fracture surface appearance; see Figure 6a.

Under less severe triaxial stress conditions, e.g., as in smooth ($R/\rho = 0.0$) and B-Notch ($R/\rho = 0.5$), the transverse-oriented material exhibits strain-to-failures which are strongly sensitive to triaxial stress (Region I), but these specimens do not show evidence of "void-sheet" induced failure; see Figure 7. In this case, fractography shows that "layering" is absent, and the fracture path appears more planar. Although, aligned and parallel elongated voids are still readily visible, roughly equiaxed voids are also present and void sheeting does not develop. Failure in this case appears to be due to general damage accumulation in the form of void growth and coalescence.

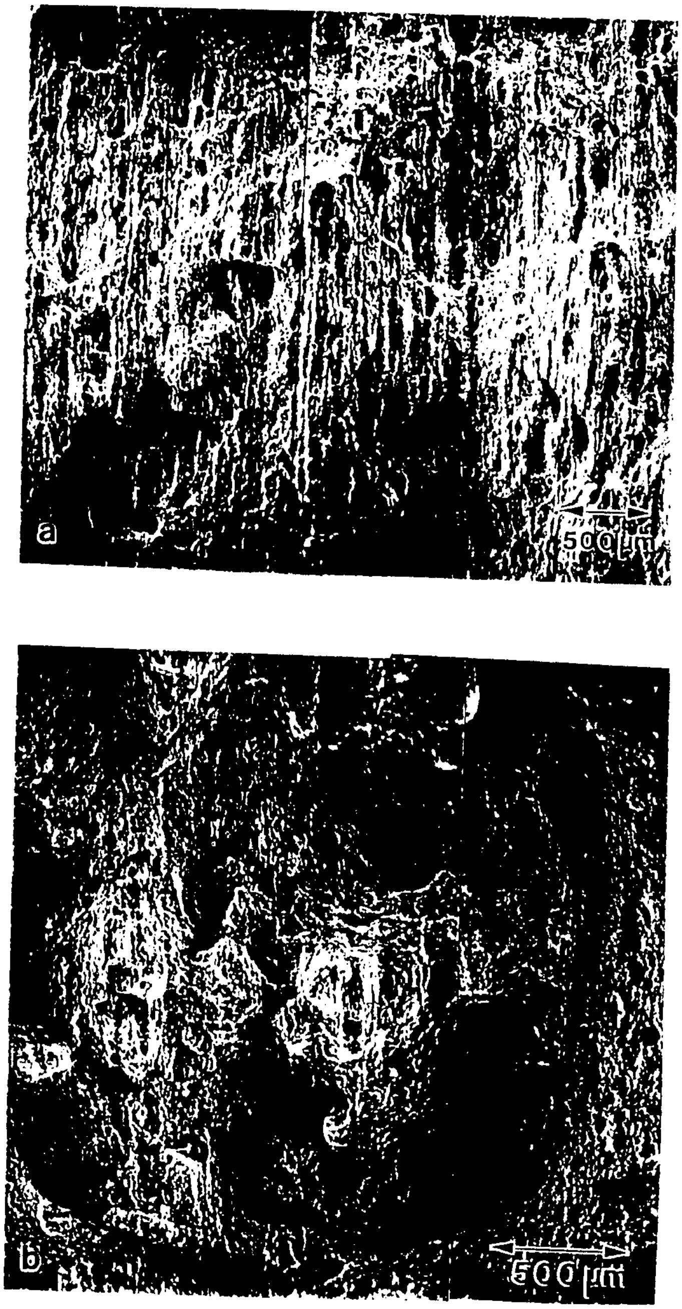

Figure 6. (a) Low magnification scanning electron micrographs illustrating the "layered" or "zig/zag" fracture surface appearance of a transverse-oriented, D-Notch (R/ρ = 2.0) base metal specimen. (b) Low magnification scanning electron micrograph illustrating the absence of the "layered" fracture surface appearance of a transverse-oriented un-notched (R/ρ = 0.0) base metal sample

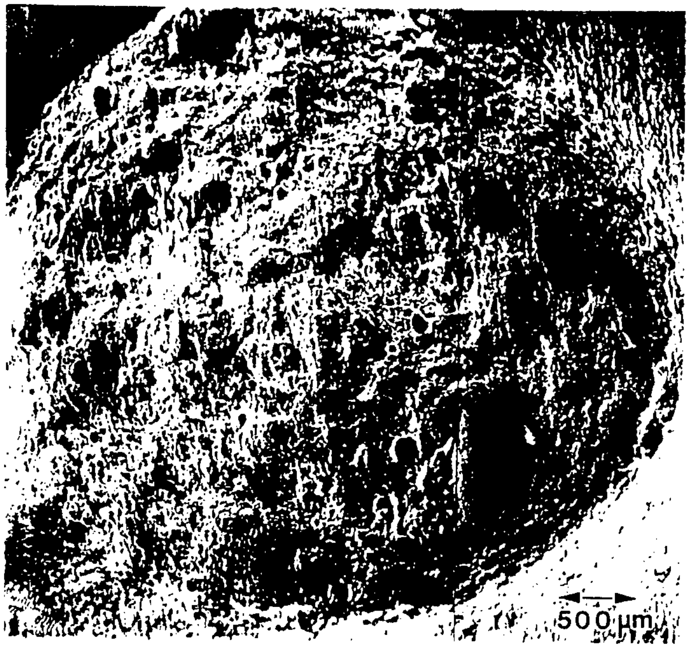

Figure 7. Low magnification scanning electron micrograph illustrating the fracture surface of a longitudinal-oriented D-Notch (R/ρ = 2.0) base metal sample.

In Plate 1-Longitudinal and Plate 2-Transverse notched round bar specimens (B-Notch, A-Notch and D-Notch), fracture surfaces also do not show evidence of "layering" or void sheeting. Furthermore, as expected from plate orientation or inclusion shape control effects, fracture surfaces are covered by roughly spherical voids (no elongated voids), and failure appears to initiate by microvoid growth and linking (Region I failure).

A comparison of the Region I data in Figure 5 suggests similar sensitivities of strain-to-failure to stress triaxiality among all materials. This similarity implies failure by a similar mechanism: global damage accumulation by void growth and coalescence. The "void-sheet" failure process observed at high triaxiality in the transverse - Plate 1 material is not observed in Region I.

Issue of Failure Initiation in Smooth Un-Notched Round Bars

An analysis of failure limit diagram data of smooth un-notched tensile specimens indicates that damage accumulation in these bars occurs over a relatively large range of triaxialities. As shown in Figure 8, following the onset of diffuse necking ($\sigma_m/\sigma_{eff} \approx 0.33$) in an initially smooth specimen, voids continue to nucleate, grow and link under continuously changing stress triaxiality, up to failure initiation at $\sigma_m/\sigma_{eff} \approx 0.85$. Therefore, the observed failure strain (and damage accumulations) reflects a wide-range of stress-states.

We are in the process of addressing this issue via interrupted smooth bar tensile testing. In our proposed testing procedure, we plan to interrupt tensile tests at a point corresponding to a relatively low triaxiality level at the bar center, e.g., $\sigma_m/\sigma_{eff} \approx 0.50$. Following removal of the neck by re-machining, the specimen will be re-deformed. This process will continue until the onset of failure.

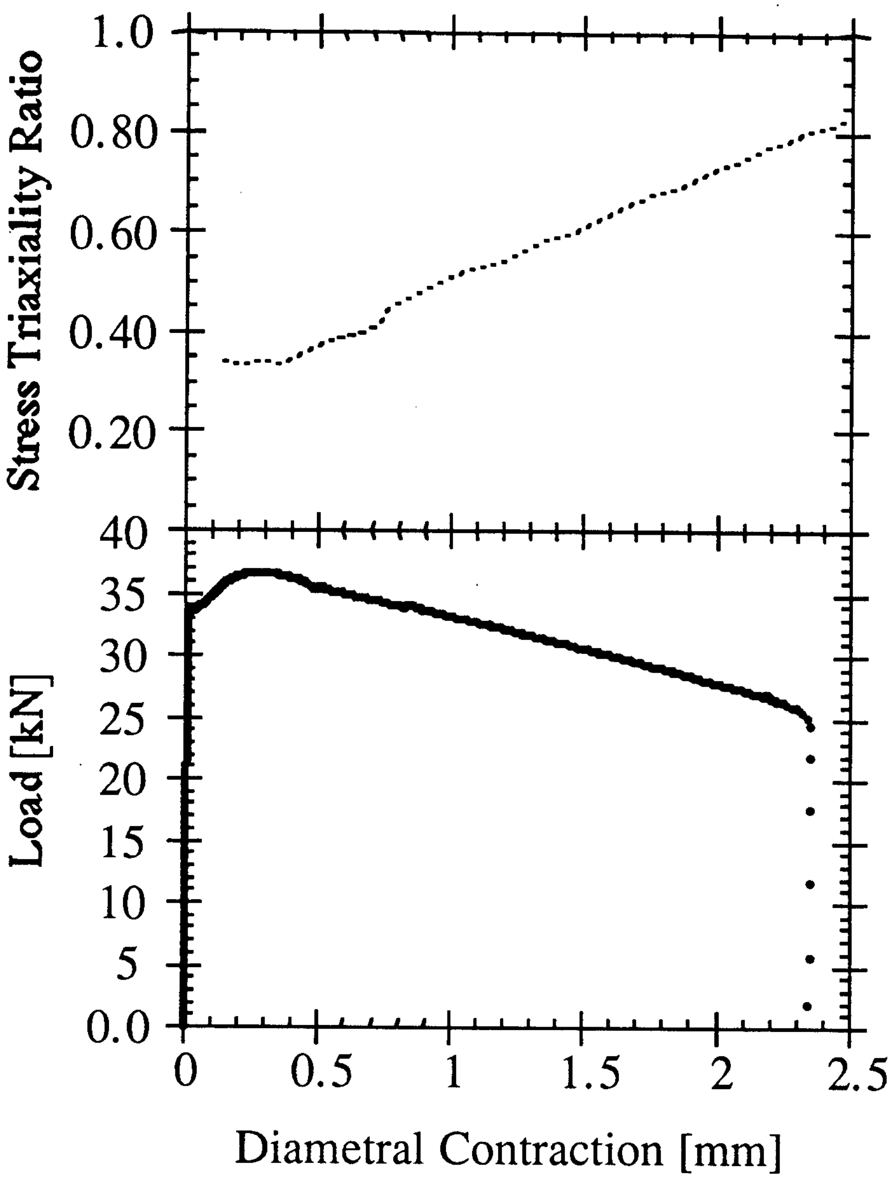

Figure 8. Load-diametral contraction response of an un-notched smooth tensile bar, and the corresponding equivalent plastic strain-stress triaxiality ratio evolution at the bar center

Heat-Affected Zone (HAZ) Material

Two regions characteristic of multipass HAZs were simulated via Gleeble thermal cycle simulations. The regions, referred to as the coarse grain HAZ (CGHAZ) and the partially re-austenitized HAZ (PRAHAZ), were produced to simulate two different microstructural conditions within the HAZ. Figures 9 and 10 illustrate the thermal histories of the CGHAZ and PRAHAZ, respectively. These thermal histories were chosen based on a computational model of thermal profiles (and therefore microstructural evolution) in multipass welds proposed by Reed and Bhadeshia (ref).

The CGHAZ created during the simulated multipass welding procedure consisted of three thermal cycles. The first cycle raised the peak temperature of the base metal to ≈1300°C ($T_{peak} >> A_{c3} \approx 823°C$), and acts as the grain coarsening step. The second cycle raised the peak temperature to ≈1060°C ($T_{peak} > A_{c3}$),while the peak temperature is within the region where grain refinement due to recrystallization occurs. No effort was made in our study to investigate the evolution of the microstructure following this second cycle. The peak temperature achieved by the third cycle is below the experimentally determined A_{c1} temperature for HY-100 ($A_{c1} \approx 700°C$), and therefore is expected to act as a tempering step.

To simulate the PRAHAZ, two thermal cycles were required. The first cycle raises the peak temperature to ≈ 760°C, which corresponds to a temperature in the ferrite+austenite phase field ($A_{c3} > T_{peak} > A_{c1}$). This cycle acts to partially re-austenitize the base metal as well as to temper the untransformed portion of the base metal. The second cycle, to ≈ 650°C, provides tempering of the previously transformed and untransformed base metal.

Failure Limit Diagram of the Simulated HAZ Material

Utilizing an analogous method to identify the onset of failure and to calculate local stress and strain values within the notch as that used in the base metal portion of this study, a failure limit diagram for CGHAZ and PRAHAZ material was constructed; see Figure 11. In all cases, the specimens are oriented in the transverse direction. To date we have only tested notched bars in

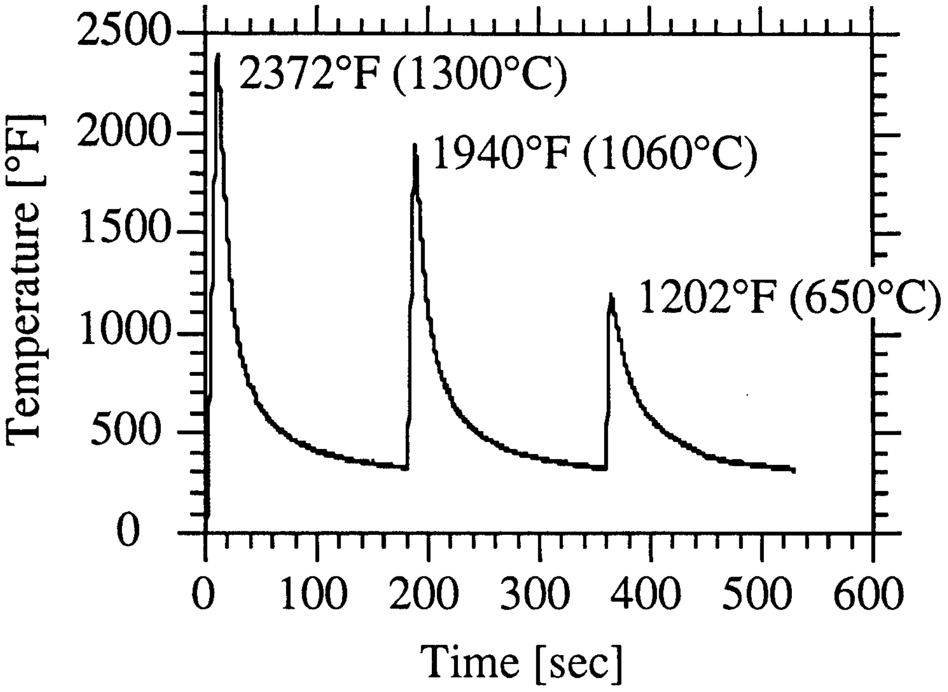

Figure 9. Thermal history of simulated coarse grain heat-affected zone material (CGHAZ) produced using a Gleeble thermal cycle simulator

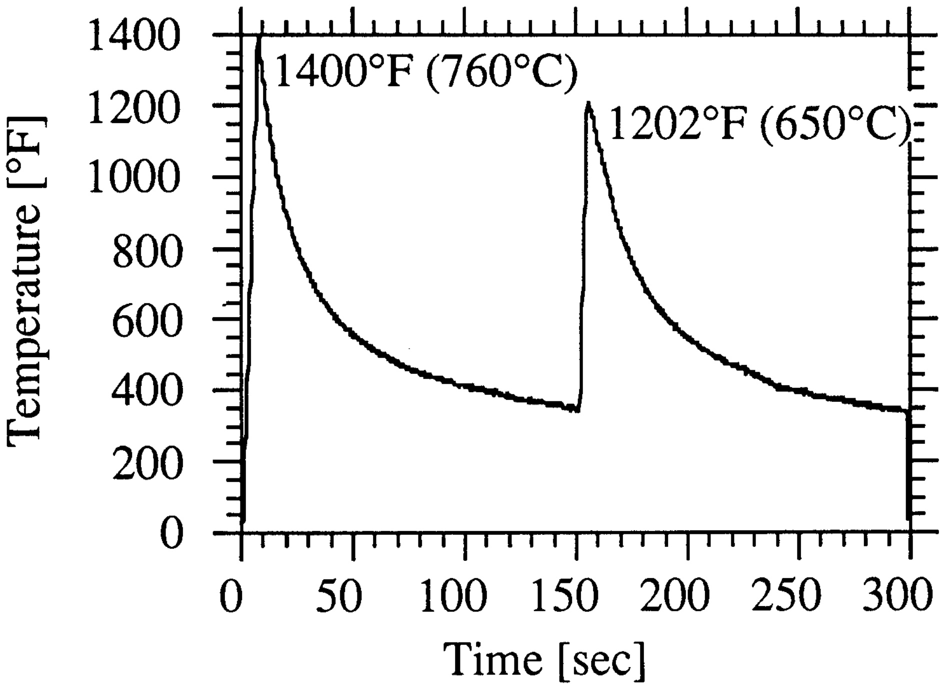

Figure 10. Thermal history of simulated partially re-austenitized heat-affected zone material (PRHAZ) produced using a Gleeble thermal cycle simulator

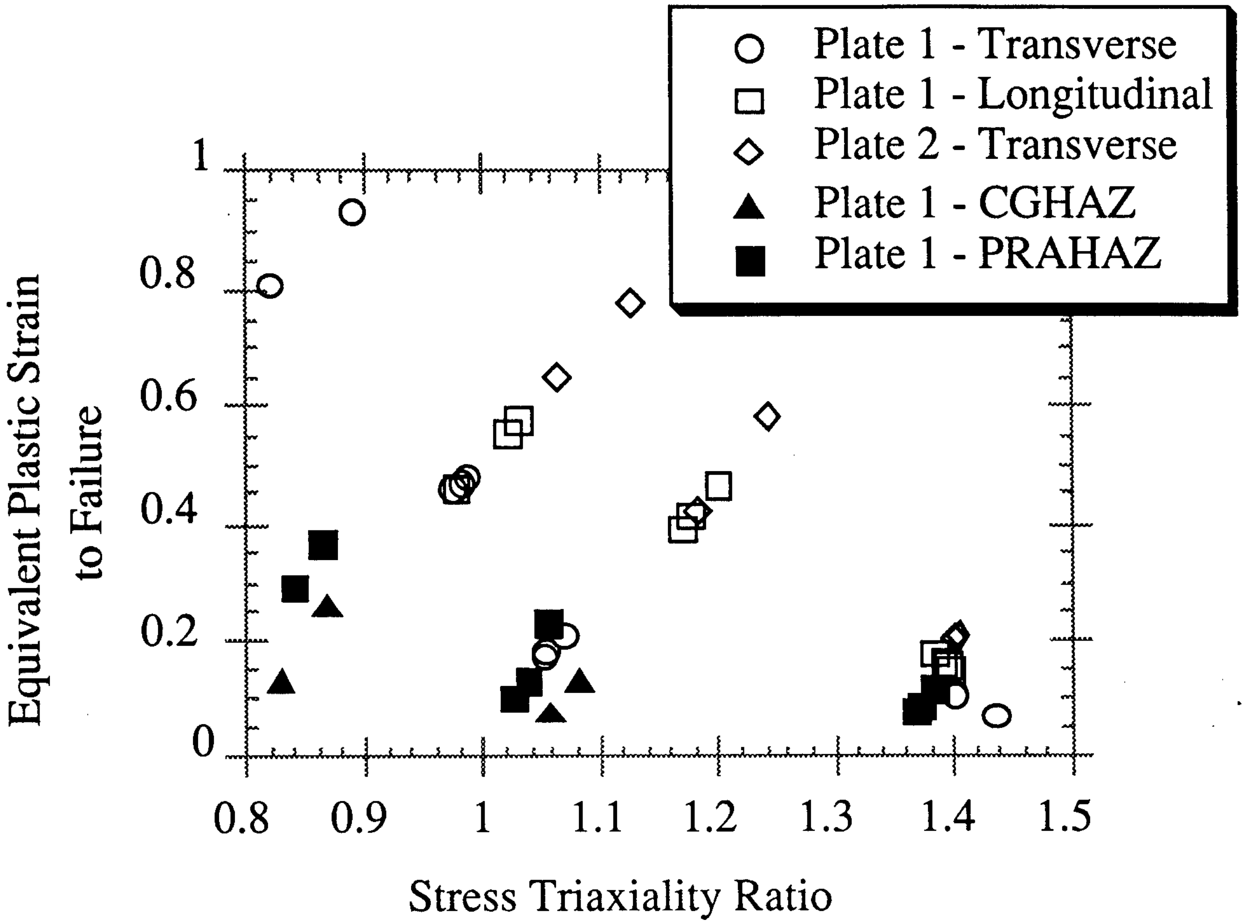

Figure 11. Failure limit diagram for simulated HAZ materials. Base metal failure data is superimposed on HAZ data for the purpose of comparison

light of the remaining issue regarding damage evolution and failure initiation in smooth tensile bars (see the previous discussion).

Our preliminary failure limit diagram data show that the simulated HAZ material exhibits behavior at high stress triaxiality which are comparable to those of the parent Plate 1-Transverse base metal. At intermediate triaxialities, such as the B-Notch ($R/\rho = 0.5$) configuration, the failure data are significantly lower than that of the B-Notch Plate 1-Transverse material. In addition, the failure strain appears relatively insensitive to stress triaxiality over the entire range of notch configurations tested (B-Notch, A-Notch and D-Notch). This behavior is similar to that of the Region II behavior of the Plate 1-Transverse material at high triaxial stress levels where void sheeting was observed. Based on this observation, a schematic representation of the expected failure limit diagram is illustrated in Figure 12. Fractography still needs completed to confirm the presence of the void-sheet mode of failure. Figure 12 anticipates that the failure loci for simulated HAZ material will be offset from the base-plate locus to lower values of triaxial stress and that the transition in the sensitivity of the failure strain to $\sigma_m/\bar{\sigma}$ will be shifted to lower values of triaxial stress.

Implications and Future Work

The above experimental results contain several implications and requirements for future work. These are as follows:

(a) The low sulfur content and inclusion-shape control of Plate 2 has an appreciable beneficial effect on ductility under low to moderate levels of stress triaxiality. Compare to convential base plate material (Plate 1), failure is retarded significantly. Similarly, as expected, the failure strains of Plate 1 in the longitudenal direction are significantly higher than in the transverse direction. However, at the most severe imposed triaxial stress condition, i.e., D-Notch (R/ρ = 2.0), the failure data converge. Thus at high stress triaxialities, plate chemistry and specimen orientation have surprisingly little influence on the failure initiation strain.

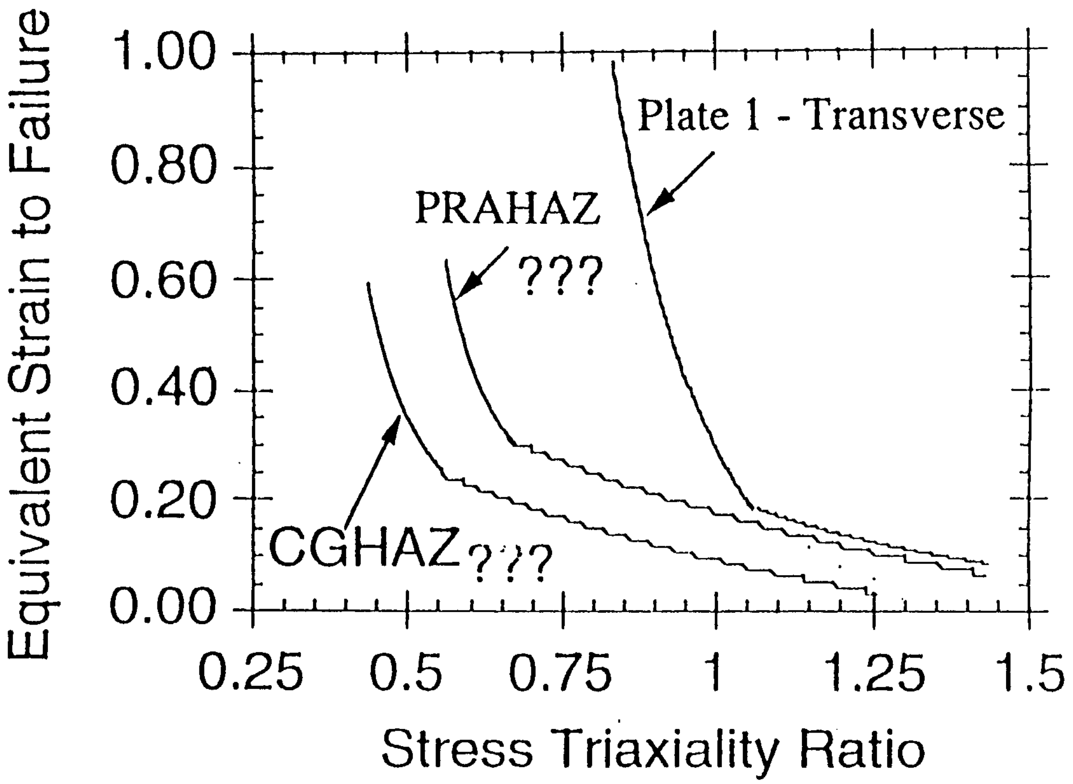

Figure 12. Anticipated failure limit diagram for HAZ materials. This figure illustrates the expected sensitivity of strain-to-failure on stress triaxiality for HAZ materials, based on the failure limit diagram behavior for transverse-oriented base metal.

(b) The failure limit diagram data and fractographic observations of Plate 1-Transverse specimens suggest a transition in the failure mechanism from global microvoid growth and linking to localized "void-sheet" failure at high stress triaxiality ratios > 1. The cause of this transition is not understood. However, the relatively weak stress sensitivity of the void-sheet failure process is consistent with a computational model described in the next section. Our current observations suggest that all failure conditions which exhibit strong sensitivities of failure strain on triaxial stress appear to fail by microvoid growth and linking.

(c) The issue of failure initiation under conditions of low stress triaxiality ($\sigma_m/\sigma_{eff} \leq 0.5$) has yet to be resolved. We plan to assess the interrupted smooth bar tensile testing scheme outlined as to its viability as a practical method by which the range of triaxial stress encompassed within the center of the neck can be minimized.

(d) At high stress triaxialities, the preliminary failure limit diagram data for the simulated HAZ material are comparable to the corresponding base metal, which is Plate 1 tested in the long transverse orientation. However, the HAZ data and that the transition between failure mechanisms is similarly shifted to lower triaxial stress , especially for the CGHAZ material. Smooth bar testing will be performed once we have resolved the smooth bar failure issue referred to in (c). Completion of the notched bar tests and fractography is expected in the near term.

(e) To better understand the failure mechanism, the damage states prior to and at failure initiation are being studied. Test deformed up to the point of failure initiation at room temperature have been subsequently fractured at high strain rates at -196°C. As expected the fracture surface displays two distinguishable regions : ductile fracture damage characteristic of room temperature failure initiation and cleavage caused by the subsequent low temperature fracture. Preliminary results indicate that the projected area fraction of microvoid fracture at failure initiation is less than 0.05 for B-, A- and D-Notched specimens. Smooth, un-notched bars have not yet been analyzed. Metallographic sections indicate planar void area fractions of ≈ 0.01. Thus, even though the fracture path selects zig-zag planes of high void content, the damage level sufficient to initiate failure ("self-propagating damage") is quite low when compared to spheroidized steels, where void volume fractions (measured from planar sections) are usually in the 0.05 to 0.15 range at fracture.[12,13]

2. SIMULATION OF THE VOID SHEET MODE OF FRACTURE
(with James Bandstra, Ph.D. Candidate)

Introduction

From the previously described experimental evidence for the tensile fractures of HY-100 in the LT orientation at high stress triaxialities, the mechanism of ductile fracture appears to be the nucleation and growth of void sheets between a relatively low void volume fraction (< 1%) of MnS elongated inclusions. Such a damage level is not sufficiently high for failure due to global void coalescence. The MnS nucleated voids at a size of 2-3 μm (the thickness of MnS inclusions) and grow to 5 - 15 μm and final fracture occurs in a zig-zag void sheet fashion with a localized crack or failure between these large voids at approximately 45 degrees from the tensile axis. The large elongated voids are approximately 70 μm apart from center to center. It appears from examination of the failure surface between these large voids, that the final fracture, which occurs over a small increment of far-field strain, is caused by void nucleation and sudden growth and coalescence associated with carbide particles (0.2 - 1.0 μm diameter) lying in a plane of highly localized plastic strain connecting the larger voids. This is consistent with other studies[5,10,11] involving high strength steels. In order to study this type of strain localization and void sheeting mechanism and its dependence on stress state, finite element simulations were performed on a microstructure simulating the local failure process. The purpose of the FEM simulation is to determine if the micromechanism of elongated MnS-nucleated voids could lead to an intense strain localization between the large voids which in turn could trigger nucleation of microvoids at Fe_3C particles in the localized region and thus account for the fracture of the material.

FEM Model

The finite element model for this simulation consisted of a 3 mm by 3mm block of HY-100 with either 2 or 6 circular voids of 2.5 μm diameter (roughly the thickness of MnS inclusions) inclined on a line 45 degrees from the tensile axis. The center to center spacing of the voids was 70 μm, which corresponds to MnS inclusion spacing as determined from fractography of notched HY-100 specimens. The model was analyzed in plane strain using the ABAQUS finite element program. The matrix material was modeled using the stress-strain data for HY-100 (Plate 1) determined in this effort. The overall mesh is shown in Figure 13. The 2 hole model contained 4300 6-noded triangular elements (ABAQUS CPE6 elements) with a close-up of the hole region given in Figure 14. The 6 hole model contained 10830 6-noded triangular elements with a close-up picture of the hole region in Figure 14. The 6 hole model is intended to represent a cluster of inclusions in the special 45 degree orientation. The large number of elements was needed both to model the holes in sufficient detail with a fine mesh surrounding the holes and to analyze a large enough piece of material so that edge effects would not distort the local effects. The bottom of the block was fixed in the vertical direction. The nodes on the top of the block were constrained to move together in the vertical direction through the use of constraint equations. Similarly, the right and left hand vertical sides were constrained to remain vertical. To assess the effect of stress triaxiality that was present in the actual experiments with the various axisymmetric notch geometries, the model had different normal stresses applied on the top surface and the side surfaces to vary stress biaxiality in this plane strain case. With the horizontal direction denoted as "1" and the vertical direction denoted as "2", the following stress biaxialities were imposed on the 2 and 6 hole models: 0.3, 0.45, and 0.6.

Results and Discussion

The specific purpose of the analysis is to examine the effects hole number (2 holes vs. 6 holes) and stress biaxiality on the localization of strain between the holes and to ascertain whether

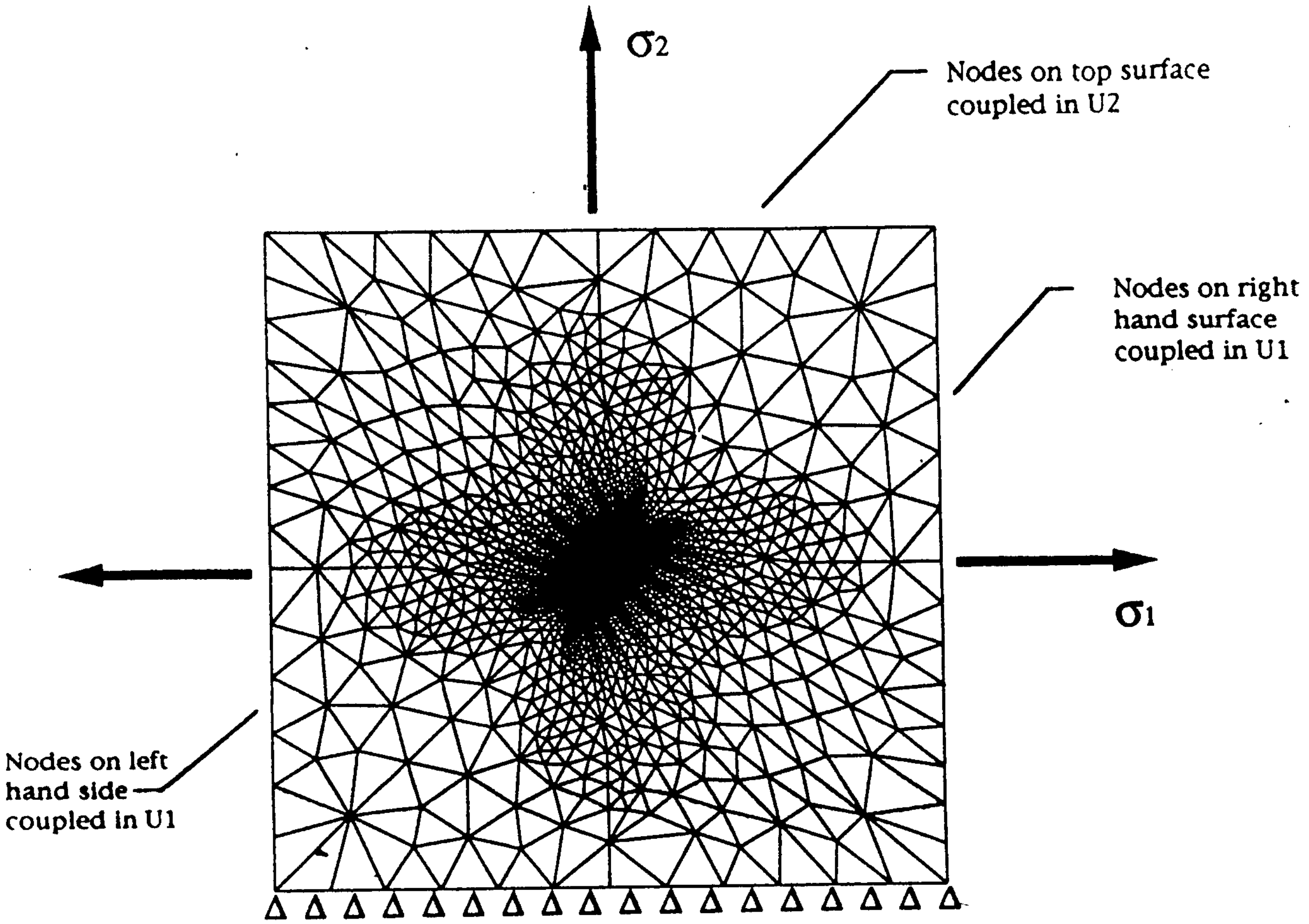

Figure 13. The finite element model for a specimen with 6 holes.

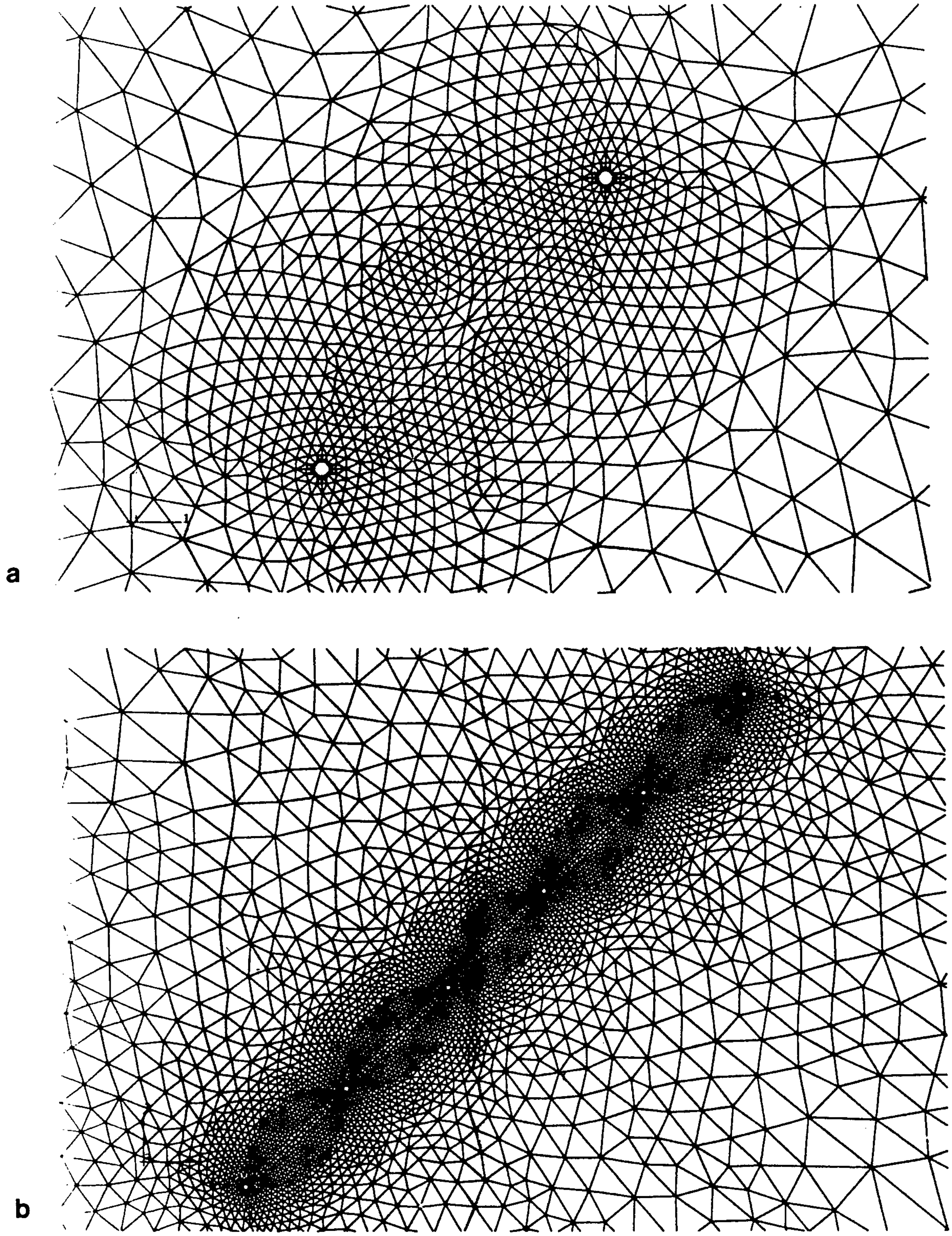

Figure 14. The mesh in the region of the holes for (a) the two-hole model and (b) the six-hole model.

the proposed strain localization with carbide void sheeting was a realistic model for the ductile fracture of HY-100 steel. The analyses were performed in plane strain to simulate the plane of zero extension that can develop between properly oriented parallel, long voids. The results focus on the relation between localized strain and far-field strain. Localized strain is determined at the center of the location between the center-most holes. Far-field strain is taken from a region far from the effects of the holes. All strains reported are equivalent plastic strain.

Initially, simulations were performed with voids having an initial diameter of 10 μm, and the far-field strain needed to obtain a localized strain high enough to initiate carbide void nucleation was determined.[+] The effect of growing the voids from the initial 2.5 μm diameter size was therefore not included in the initial analysis. This growth effect of the MnS voids was first examined by adding a growth strain calculated using the method of McClintock[14]. A comparison of the two analyses shows that the total far-field strain needed to achieve strain localization high enough to cause carbide microvoid nucleation was found to be dominated by the McClintock growth strain of the large voids. Thus, this approach was abandoned and replaced by a FEM simulation based on an <u>initial</u> void size of 2.5 μm.

The finite element analyses performed with circular voids that were initially 2.5 μm in diameter and grew to approximately 10 μm approximate the growth of cracked or decohered MnS inclusions (that begin at approximately 2.5 μm thickness) to 10 μm voids. Analyses were performed for stress biaxialities S_1/S_2 (where S_1 and S_2 are principal stresses) of 0.3, 0.45, and 0.6, and plane-strain conditions were assumed along the hole axes. Figure 15 shows an example of intense strain localization between the two innter-most holes in a six-hole array. The evolution of strain localization are plotted in Figure 16 for both the 2 hole case and the 6 hole case. As is evident from these figures, increasing stress biaxiality markedly accelerates the strain localization process. Increasing the hole number from 2 to 6 has an additional effect of promoting strain localization (compare Fig's 16a and 16b). The plane-strain far-field strain values which result in a critical localized carbide nucleation strain of 0.5 are given in Table I.

[+] Based on previous research,[12,13] we shall assume that microvoids initiate at carbides at equivalent strains of ≈ 0.5.

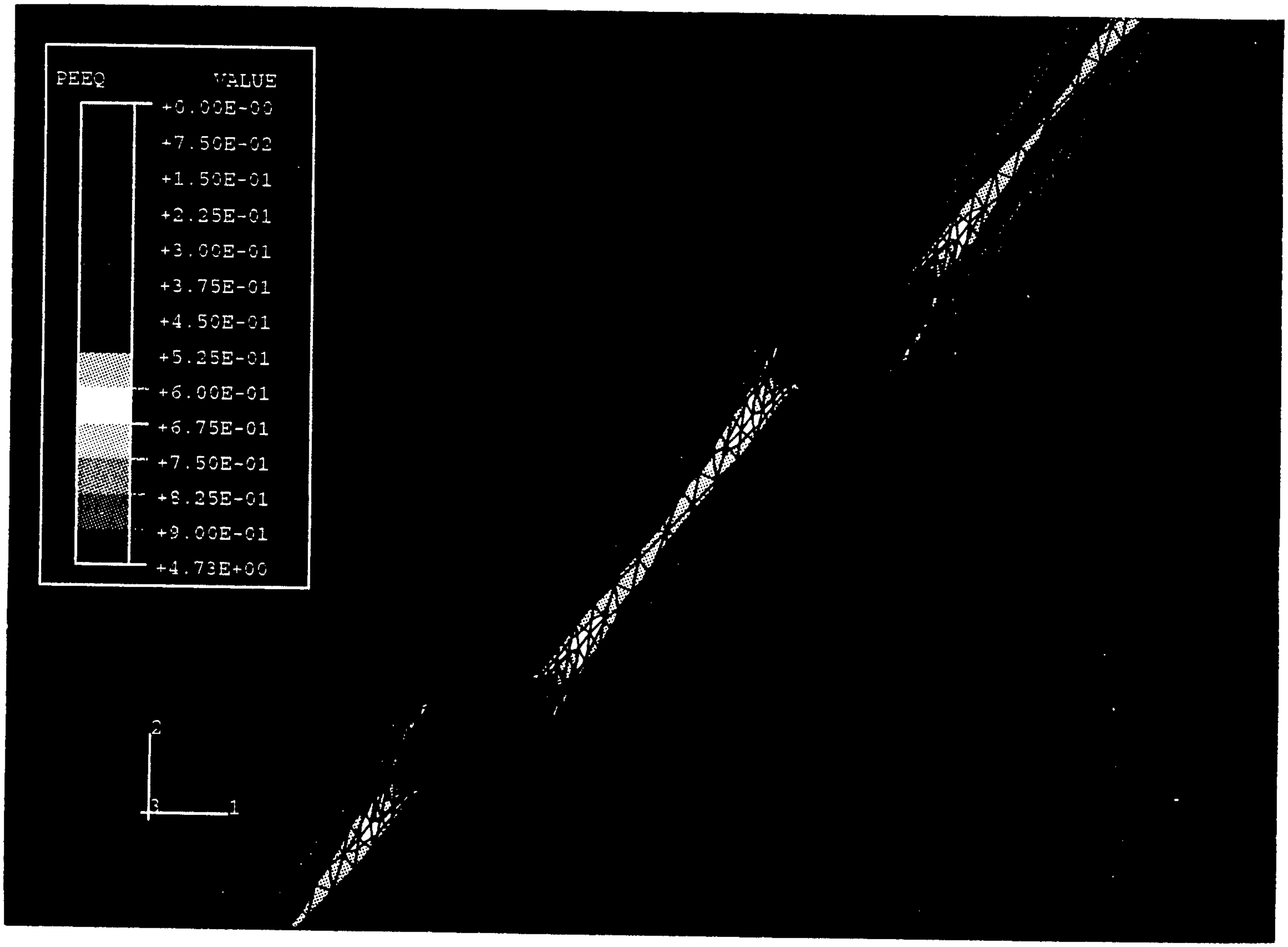

Figure 15. Strain localization in terms of equivalent plastic strain contours between the two inner-most holes of a six-hole array strained at $S_2/S_2 = 0.45$. Note that the holes have grown from 2.5 µm to ~10 µm diameter.

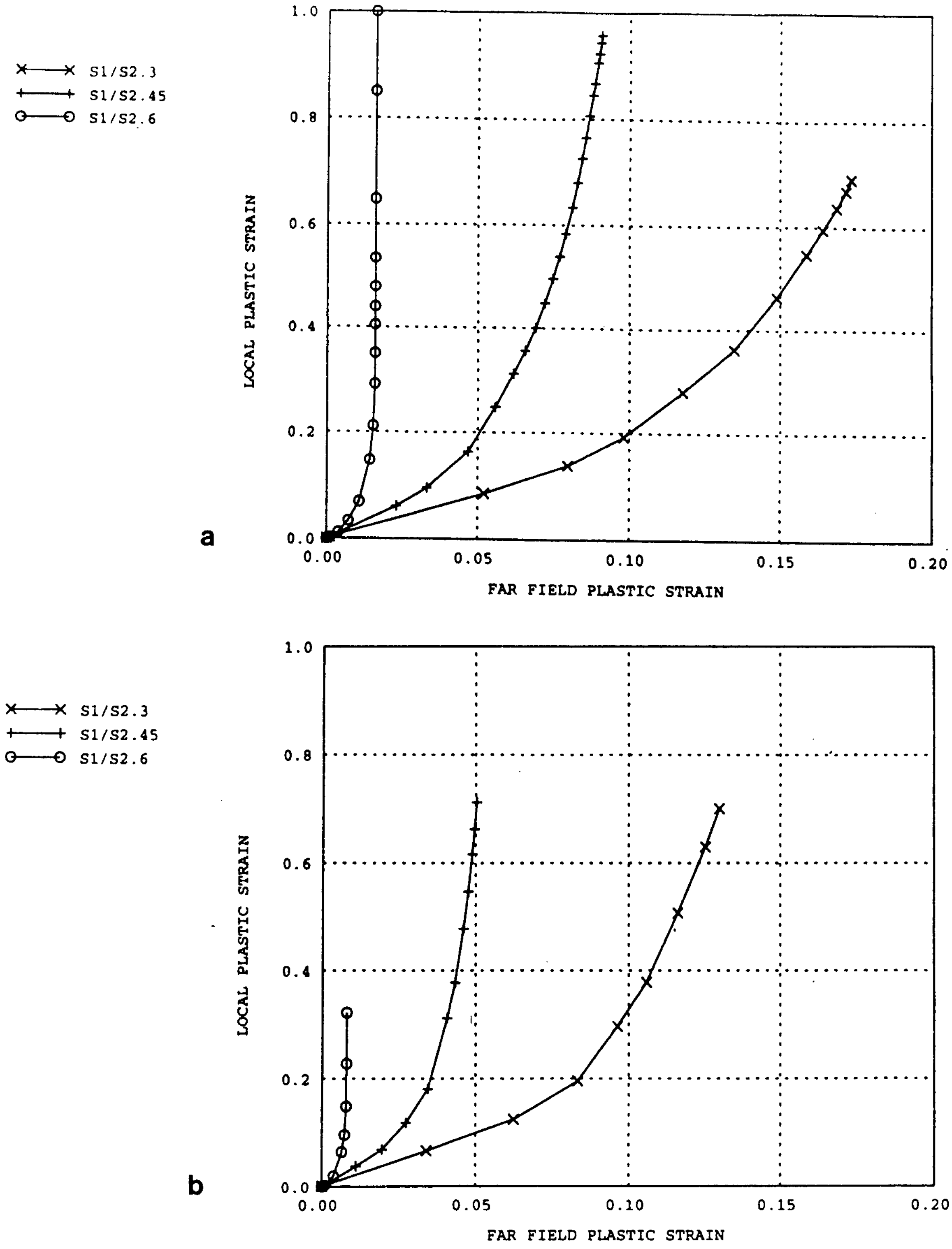

Figure 16. The local equivalent plastic strain as a function of the far-field plastic strain for three stress biaxialities, S_1/S_2. (a) shows behavior for 2 hole model while (b) shows results for 6 hole model.

If we assume that carbide-initiated microvoids nucleate at local equivalent strains of ≈ 0.5, the data in Figure 16 may be used to obtain a plane-strain far-field "failure" strain values which result in the critical carbide nucleation strain of 0.5. It should be noted that the nature of the strain localization process makes our prediction of a far-field failure strains relatively insensitive to the precise choice of microvoid nucleation strain. As expected, Table I shows a decrease in failure strain with increasing stress triaxiality and hole number.

Table I Far Field "Failure" Strain at Interhole Microvoid Nucleation Strain as a Function of Stress Biaxiality, S_1/S_2.

S_1/S_2	2 HOLE	6 HOLE
0.3	0.155	0.116
0.45	0.075	0.047
0.6	0.016	0.0079

Even though our simulation treats elongated voids as through-thickness cylindrical holes, it is instructive to compare predicted failure strains with those experimental observed for Plate 1-transverse, notched tensile specimens. Figure 17 shows that the predicted failure strain compare well with those experimentally determined. Not only are the predictions of the correct order of magnitude, but also the relatively small sensitivity of the void sheeting to stress state is correctly described. Implicate in the above comparison is the assumption that the strain to nucleate the elongated MnS voids is negligibly small; we believe this is reasonable.

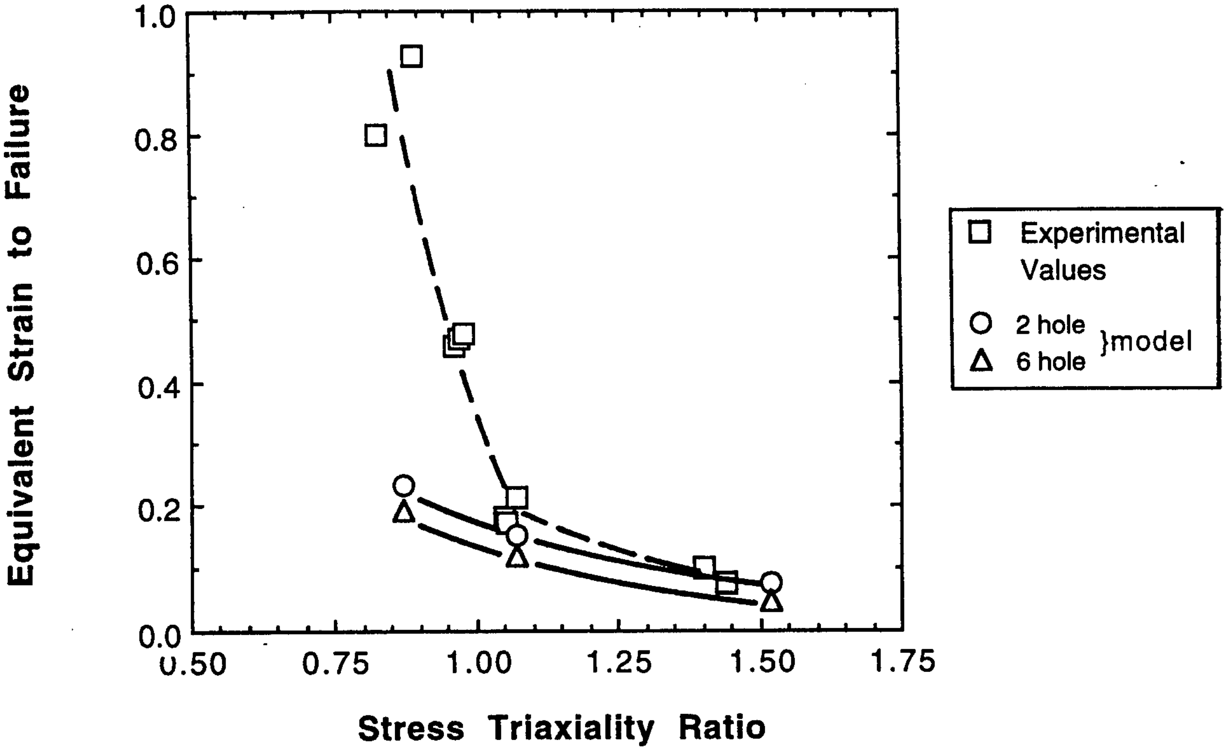

Figure 17. Predicted and observed failure limit diagrams for the void-sheet mode of failure in HY100 steel baseplate.

Summary

The present computational model depicts a void-sheet mode of ductile fracture which is relatively insensitive to stress triaxiality similar to that observed experimentally. The analysis indicates that, upon nucleation of elongated, 2.5 μm-diameter voids at properly oriented MnS inclusions, the subsequent void growth (to $\simeq$ 10 μm) and concurrent strain localization between these voids results in failure at far-field strain levels which are comparable to those measured both in magnitude and stress-state sensitivity. However, as seen from Figure 14 at stress triaxialities less than approximately 1, the proposed void sheeting model predicts a much lower failure strain than test data indicate. As discussed earlier, it is at roughly this stress triaxiality that void sheeting is replaced by a failure mechanism dependent on the sustained growth and coalescence of relatively equiaxed voids on a more global scale. Nucleation and growth of elongated hole-shaped voids at MnS inclusions at low stress triaxialities does not appear to occur despite the continued presence of the MnS inclusions. Failure by this latter mode, which is very sensitive to stress state, needs to be addressed in the future.

3. AN EXPERIMENTAL MODEL OF THE GROWTH OF NEIGHBORING VOIDS DURING DUCTILE FRACTURE

(with D. M. Goto, Ph.D. Candidate)

Introduction

Ductile fracture of metallic alloys usually involves global damage accumulation in the form of microvoid nucleation, growth, and coalescence. This process dictates failure in our materials except for the intervention of void sheeting in Plate 1-transverse material at high stress triaxialities. In some alloys, voids are nucleated at strains which are relatively small in comparison to the fracture strain; in these cases the ductile fracture process is controlled by void growth and linking. The growth of an isolated, non-interacting spherical void was originally modeled by Rice and Tracey and subsequently verified using computational methods by others[15-17]. Several studies have indicated that the predicted growth behavior of isolated voids is in good agreement with experimental observations at "small" void volume fractions; see refs. 18 and 19 for reviews. However, ductility predictions based on non-interacting voids predict unrealistically large failure strains, and void interactions and accelerated thinning of the intervoid ligament are thus expected at "large" volume fractions of voids.

In the present study,[20] we utilized a novel specimen geometry to model the growth and interaction of neighboring voids during deformation. As shown in Figure 18, the specimen uses pairs of blind-end holes with hemispherical ends to monitor the deformation behavior of the inter-hole ligament. Our key assumption is that, in the blind-hole specimen, the strain-induced thinning behavior of the inter-hole ligament is similar to that of the ligament between a pair of neighboring spherical microvoids spaced a similar distance apart. The experimental advantage of our approach is that the minimum ligament width can be directly and accurately measured as a function of specimen strain. Such data permit a straight-forward quantification of void interaction effects as a function of intervoid spacing and applied strain.

Results and Discussion

The dependence of inter-hole ligament thinning on axial strain, ε_1, is shown in Figure 19. These data, which are based on copper specimens, are normalized to the initial inter-hole ligament width W_o, and show that, as expected, the ligament thins with increasing strain. Somewhat unexpected is the observation that the rate of thinning, $d(W/W_o)/d\varepsilon_1$, increases with decreasing interhole spacing W_o. In addition, the rate of thinning, while nearly linear with strain for holes spaced 2.0D apart, appears to accelerate with strain for the 0.5 D and 1.0 D cases. It should be noted that the data in Figure 19 comprises three tests for each condition with experimental scatter ($3\sigma = \pm 0.015$) being less than the size of the data point. Measurement of ligament thinning at larger strains was precluded by the intervention of fracture before the ligament could thin to a "knife-edge"; thus, coalescence of the hole-ends was not achieved.

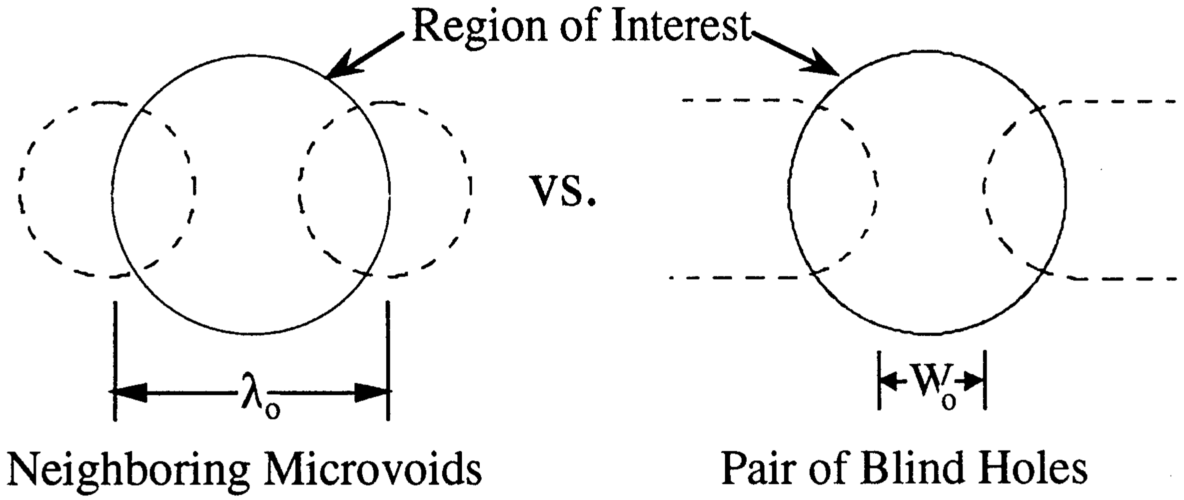

Figure 18. A model of the interaction between neighboring microvoids by a pair of blind holes.

In order to interpret the data presented in Figure 19, we may compare the observed ligament thinning behavior to that expected of a ligament between a pair of isolated, non-interacting voids initially spaced either 0.5 D, 1.0 D, or 2.0 D apart. Note that agreement between predicted and observed ligament thinning would indicate that the hole ends behave as non-interacting voids.

To predict the contribution to thinning from the growth of a pair of non-interacting, initially spherical voids, we model void growth by the Rice-Tracey model[15,19]. This model predicts the transverse void diameter, d, as a function of the major principal strain ε_1, as :

$$d = \left[e^{D'\varepsilon_1} - \frac{5}{6D'} [e^{D'\varepsilon_1} - 1] \right] \; d_0 \qquad (1)$$

where d_o is the initial diameter, and $D^{'}$ is a constant which depends weakly on strain hardening but is sensitive to stress triaxiality. For uniaxial tension (stress triaxiality = 1/3) and Cu (strain hardening exponent $n = d\ln\sigma/d\ln\varepsilon \approx 0.4$), the value of D' is approx. 0.25. The void growth relation, Eq.1, predicts that in uniaxial tension void growth causes a void shape change from spherical to ellipsoidal, with an increase in the longitudinal dimension and a corresponding decrease in the transverse dimension. By itself, this relation predicts, as a result of transverse contraction of the void, an increase in inter-hole ligament width with increasing ε_1.

However, the voids are embedded in a uniaxial tensile field which displaces the void centers toward each other during uniaxial tension by the relationship

$$\lambda = \lambda_o \, e^{-0.5\varepsilon_1} \qquad (2)$$

where λ_o and λ are the initial and final distances between the centers of a pair of neighboring voids embedded in a plastically isotropic material; Figure 14 depicts λ_o. Therefore the overall effect of the uniaxial tensile field on ligament thinning can be represented as :

$$W = \lambda_o e^{-0.5\varepsilon_1} - \left[e^{D'\varepsilon_1} - \frac{5}{6D'} [e^{D'\varepsilon_1} - 1] \right] \quad d_0 \qquad (3)$$

Figure 19 shows a comparison of the predictions of inter-hole ligament thinning, Eq. 3, with the experimentally measured values. Such a comparison shows that for hole-ends spaced two hole diameters apart (the 2.0 D case), there is good agreement at small strains ($\varepsilon_1 \geq 0.15$) although small deviations begin to develop at larger strains. For closely spaced holes ($W \leq 1.0$ D), deviations between predicted and observed ligament thinning begin at progressively smaller strains and are quite pronounced at $\varepsilon_1 \geq 0.2$.

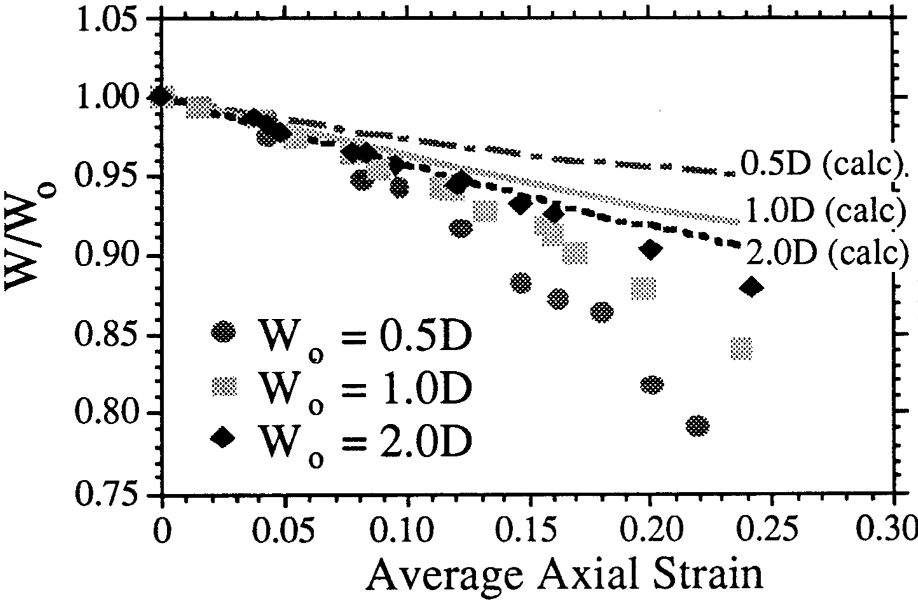

FIG 19. Ligament thinning as a function of average axial strain. Individual points corresponds to experimental test data. Lines correspond to calculated ligament thinning based on a Rice and Tracey void growth model.

We interpret the above behavior as an indication that void interaction effects occur even in this uniaxial tension case; the severity apparently depending on a combination of intervoid spacing and strain. Void interaction effects become increasingly pronounced with increasing strain and decreasing intervoid spacing. The result is that deformation causes the interhole ligament to thin at a rate which increases with increasing strain and decreasing hole spacing. When compared to predictions of the growth of isolated voids (based on the Rice-Tracey analysis[15,19] our results indicate void interaction effects accelerate ligament thinning and become pronounced with decreasing void spacing (≤ 1.0 D) and increasing applied strain ($\varepsilon_1 \geq 0.2$) even in uniaxial tension. It should be noted that these experiments do not agree with the only computational model of void interactions based on a regular array of voids spaced one void diameter apart.[21] We do not know if these void interactions can account for the strong influence of stress triaxiality on failure strain observed in Figure 19.

REFERENCES

1. F. M. Beremin, Metall. Trans. A 14A, 2277 (1983).
2. J. Lemaitre, Eng. Fracture Mechanics 25, 523 (1986).
3. P. Matic and M. I. Jolles, in Nonlinear Fracature Mechanics, Vol. II:L Elastic-Plastic Fracture, ASTM STP 995, (ASTM, Philadelphia) 1989, p. 82.
4. J. H. Giovanola and A. J. Rosakis Advances in Local Fracture/Damage Models for Analysis of Engineering Problems, AMD-vol. 137, (ASME, New York) 1992.
5. J. W. Hancock and A. C. Mackenzie, J. Mech. Phys. Solids 24, 147 (1976).
6. J. W. Hancock and D. K. Brown, J. Mech. Phys. Solids 31, 1 (1983).
7. G. R. Johnson and W. H. Cook, Eng. Frac. Mech. 21, 31 (1985).
8. J. N. Johnson and F. L. Addessio, J. Appl. Phys. 64, 6699 (1988).
9. A. M. Rajendran, M. A. Dietenberges, and D. J. Grove, J. Appl. P hys. 65, 152 (1989).
10. Cox, T. B. and Low, J. R. , Metall. Trans. 5, 1457 (1974), Metallurgical Transactions, 5.
11. Gudas, J. P., "Micromechanisms of Fracture and Crack Arrest in Two High Strength Steels", David W. Taylor Naval Ship Research and Development Center Report DTNCRDC/SME-87-20, Feb, 1987.
12. Goods, S. H. and Brown, L. M., Acta Metall, 27, 1 (1979).
13. Kwon, D., Scripta Metallurgica, 22, 1161 (1988).
14. McClintock, F. A., J. Appl. Mech. 35, 363 (1968).
15. J. R. Rice and D. M. Tracey, J. Mech. Phys. Solids 17, 201 (1969).
16. B. Budiansky, J. W. Hutchinson and S. Slutsky, in Mechanics of Solids (edited by H.G. Hopkins and M.J. Sewell), p. 13, Pergamon Press, Oxford (1982).
17. C. J. Worswick and R. J. Pick, J. Mech. Phys. Solids 38, 601 (1990).
18. W. M. Garrison and N. R. Moody, J. Phys. Chem. Solids 48, 1035 (1987).
19. P. F. Thomason, Ductile Fracture of Metals, p. 47, Pergamon Press, Oxford (1990).
20. D. M. Goto and D. A. Koss, Scripta Mater. (in press).
21. C. L. Hom and R. M. McMeeking, J. Appl. Mech. 56, 309 (1989).